Simultaneous enhancement of hardness and fracture resistance in aged AlCoCrFeNi high-entropy alloy coatings via mixed-powder laser cladding

Intermetallics 194 (2026) 109299

Contents lists available at ScienceDirect

Intermetallics

journal homepage: www.elsevier.com/locate/intermet

Simultaneous enhancement of hardness and fracture resistance in aged AlCoCrFeNi high-entropy alloy coatings via mixed-powder laser cladding

Yuyun Lu [a], Hui Zhang [a], Dong Hao [a], Ye Tao [a], Zhenqi Dong [a,b], Kaio Niitsu Campo [c,*], Sheng Guo [d,**]

[a] School of Materials Science and Engineering, Anhui University of Technology, Ma'anshan, Anhui, 243002, PR China
[b] Taier (Anhui) Industrial Technology Service Limited Company, Ma'anshan, 243002, PR China
[c] School of Mechanical Engineering, University of Campinas, Campinas, SP, 13083-860, Brazil
[d] Department of Industrial and Materials Science, Chalmers University of Technology, Gothenburg, SE-41296, Sweden

ARTICLE INFO

Keywords:
High-entropy alloys
Laser cladding
Mixed-powder processing
Columnar-to-equiaxed transition
Grain refinement

ABSTRACT

A complete columnar-to-equiaxed transition was achieved in an AlCoCrFeNi high-entropy alloy (HEA) coating by employing mechanically blended elemental powders during laser cladding. To assess the influence of microstructure on aging behavior, coatings produced from mixed powder (MP-HEA) and gas-atomized pre-alloyed powder (GP-HEA) were subsequently investigated after aging at 550 °C. While both conditions exhibited a BCC + B2 dual-phase structure with spinodal decomposition features, the MP-HEA showed a fully equiaxed and significantly refined grain structure. The refined microstructure was accompanied by a much finer spinodal modulation (~7.5 nm vs. ~30 nm), resulting in superior mechanical performance. The MP-HEA reached a hardness of 747 HV, 18.6% higher than the GP-HEA, and exhibited increased compressive yield strength (1013 MPa) together with improved fracture resistance. The results demonstrate that powder feedstock design provides an effective strategy to tailor microstructure and achieve simultaneous enhancement of hardness and fracture resistance in HEA coatings.

1. Introduction

Although high-entropy alloys (HEAs) can exhibit superior performance over conventional metals, the difficulties associated with their processing and the high production costs can limit their use as bulk materials. In this context, their application as coatings or thin films represents an attractive alternative, enabling the exploitation of their surface-related properties while reducing material consumption. Several studies have demonstrated the suitability of HEAs as protective coatings, highlighting their potential for increased hardness, reduced wear volume, and enhanced corrosion resistance, in addition to other advantages [1–6].

Among the available techniques for producing HEA-based coatings, laser cladding has emerged as a particularly promising approach due to its compositional flexibility, strong metallurgical bonding, and ability to generate dense coatings with refined microstructures [1–6]. Notwithstanding these advantages, the solidification conditions inherent to the process, characterized by steep thermal gradients and directional heat extraction into the substrate, tend to promote the formation of columnar dendritic grains [7]. Such microstructures often lead to anisotropy and increased susceptibility to solidification cracking [8]. Therefore, grain refinement, ideally via a transition from columnar to equiaxed growth, is essential to obtain structurally sound clads with enhanced hardness and improved tribological performance.

Homogeneity in terms of chemical composition, particle size, and morphology of the powder feedstock has been shown to strongly influence the grain size and microstructural morphology formed during solidification in laser-processed materials [9–11]. In a previous study [12], we demonstrated that two markedly distinct microstructures could be obtained in the AlCoCrFeNi HEA under identical processing conditions, depending on whether pre-alloyed powder or mechanically blended elemental powders were used. Specifically, samples produced using mechanically blended elemental powders exhibited a complete columnar-to-equiaxed transition (CET). In the present work, we show that this complete CET leads to a substantial increase in hardness while simultaneously improving fracture resistance in aged samples, which is

* Corresponding author.
** Corresponding author.
E-mail addresses: kaionc@unicamp.br (K.N. Campo), sheng.guo@chalmers.se (S. Guo).

https://doi.org/10.1016/j.intermet.2026.109299
Received 24 February 2026; Received in revised form 4 April 2026; Accepted 12 April 2026
Available online 27 April 2026

particularly relevant for tribological applications.

2. Experimental procedures

AlCoCrFeNi coatings were fabricated by laser cladding onto Q235 low-carbon steel using two powder feedstocks: a mechanically blended elemental mixture and a gas-atomized pre-alloyed powder (Taier, Anhui, China). Deposition was performed on an RFL-C6000 semiconductor laser system using identical processing parameters (laser power of 2.4 kW, spot size of 4 mm, and scanning speed of 8 mm s^{-1}). The coatings are hereafter designated as MP-HEA (mechanically mixed powder) and GP-HEA (gas-atomized pre-alloyed powder). Additional details regarding the powder characteristics are provided in Ref. [12]. Owing to inevitable substrate dilution, the resulting clad compositions were similar under both conditions but shifted toward $AlCoCrFe_2Ni$ [12].

Post-deposition aging was performed at 450-800 °C for 2 h. Phase analysis was conducted by X-ray diffraction (XRD, Bruker D8 Advance, Cu-Kα). Microstructural characterization was carried out using visible-light microscopy (VLM, Zeiss Axio Vert.A1), scanning electron microscopy (SEM, Quanta-450), and transmission electron microscopy (TEM, Tecnai G2 F20 S-TWIN). Vickers hardness was measured under 4.9 N with a dwell time of 20 s. Crack patterns generated under a 294 N load were used for qualitative fracture resistance assessment. Compressive stress-strain behavior was evaluated by instrumented nanoindentation (G200) in accordance with the testing standard GB/T 39635-2020 [13].

3. Results and discussion

Fig. 1(a and b) present VLM images of the cross-sectional microstructures in the as-deposited condition. The GP-HEA coating is mainly composed of coarse columnar grains aligned along the heat flow direction, which transition to equiaxed grains toward the top of the coating. This behavior is expected, as the temperature gradient to growth rate ratio (G/R) decreases during the advancement of the solid-liquid interface, favoring the CET. In contrast, the MP-HEA coating displays a fully equiaxed and significantly refined grain structure throughout the coating thickness. This demonstrates the importance of powder

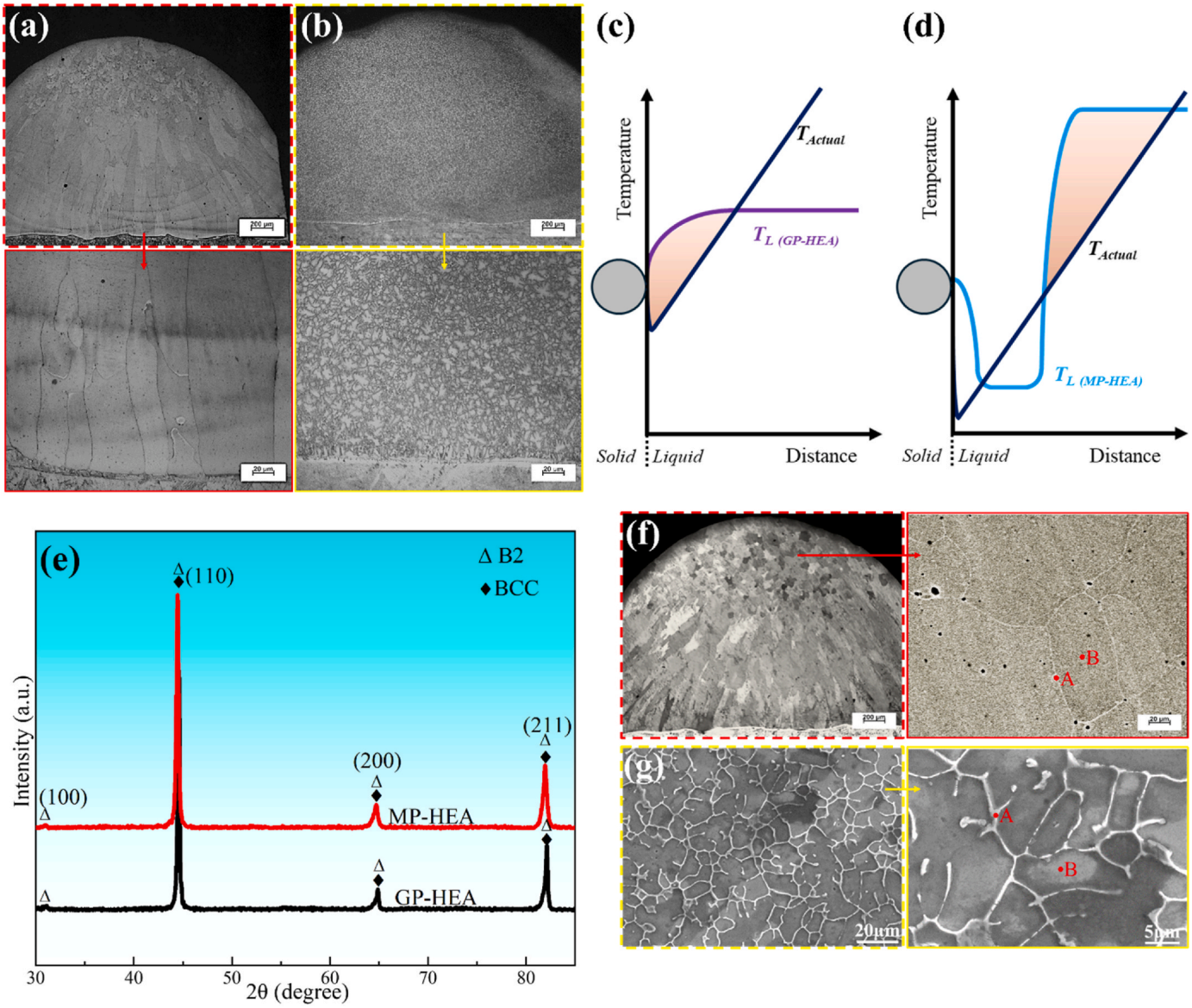

Fig. 1. Cross-sectional VLM micrographs of the as-deposited coatings: (a) GP-HEA and (b) MP-HEA. Schematics illustrating solidification under (c) homogeneous and (d) compositionally fluctuating melts. (e) XRD patterns of the AlCoCrFeNi coatings after aging at 550 °C. Microstructures after aging: (f) GP-HEA (VLM micrographs) and (g) MP-HEA (secondary electron SEM micrographs).

feedstock characteristics and their ability to induce a complete CET.

As discussed in detail previously [12], incomplete chemical homogenization arising from the use of elemental powders, combined with specific laser parameters (i.e., heat inputs insufficient to promote full mixing), can result in spatial compositional fluctuations throughout the melt. During solidification of a chemically homogeneous liquid, as achieved here using the pre-alloyed powder (GP-HEA), the liquidus temperature (T_L) increases away from the solid-liquid interface due to conventional solute gradients caused by solute pile-ups (for partition coefficient $k < 1$). This leads to constitutional supercooling, as schematically shown in Fig. 1c. However, the high thermal gradients typical of laser processing reduce the constitutionally supercooled region, favoring columnar growth.

In a melt with compositional fluctuations, on the other hand, the solute gradients can be much stronger and spatially distributed, forming regions with higher and lower local T_L. This can promote erratic nucleation behavior, as the advancing solid-liquid interface may encounter regions with lower T_L ahead, locally reducing the driving force for solidification. Under such conditions, sufficient undercooling can develop in adjacent regions with higher T_L, enabling nucleation. This solidification scenario is schematically illustrated in Fig. 1d, where local variations in T_L are represented by constant minimum and maximum values for simplicity. If alternating high- and low-T_L regions are relatively uniformly distributed throughout the melt, several nucleation events can occur, thus impeding the development of columnar grains, which likely explains the observed complete CET. Furthermore, as a result of the increased nucleation rate, the CET is accompanied by a significant reduction in grain size.

The XRD patterns of the coatings aged at 550 °C (Fig. 1e) reveal the same phase constitution, characterized by a majority of BCC phase with secondary ordered B2 phase. The presence of the (100) superlattice reflection provides clear evidence of B2 ordering. It should be mentioned that the coatings aged at 550 °C were selected for detailed microstructural characterization because this condition yielded the highest hardness, as shown later. The absence of additional diffraction peaks indicates that complete melting and alloying of the mixed elemental powders occurred during laser processing. Furthermore, after aging at 550 °C, the overall grain morphology remained almost unchanged compared to that shown in Fig. 1(a and b), as illustrated in Fig. 1f for the GP-HEA coating.

Fig. 1(f and g) exhibit the resulting microstructures after aging at 550 °C for the GP-HEA and MP-HEA coatings, respectively. The grain boundaries and interdendritic regions of the MP-HEA (Fig. 1g) appear decorated with Cr-rich precipitates, as confirmed by the SEM energy-dispersive X-ray spectroscopy (EDS) point analysis, with semi-quantitative results presented in Table 1. The aging treatment did not promote long-range diffusion, because the compositions reported in Table 1 follow trends similar to those obtained in the as-deposited condition [12]. It is interesting to note that differences in composition between points A and B (representing, respectively, grain boundaries/interdendritic areas and grain interiors) are more pronounced in the MP-HEA coating. This may be indirect evidence of compositional fluctuations in the melt, since there is no partitioning-based mechanism that would account for such differences if both HEA coatings had originated from a chemically homogeneous liquid, given they were processed under the same laser parameters.

Table 1
Typical chemical compositions of different regions (points A and B in Fig. 1(f and g)) in the MP-HEA and GP-HEA coatings aged at 550 °C, as determined by SEM-EDS.

Sample/Position		Composition (at%)				
		Al	Co	Cr	Fe	Ni
GP-HEA	A	16.8	15.4	15.4	36.1	16.3
	B	18.0	16.2	15.0	35.0	15.8
MP-HEA	A	4.8	18.2	44.5	26.5	6.0
	B	18.9	18.6	13.3	29.4	19.8

TEM microstructures (Fig. 2) reveal similar features for both HEA coatings aged at 550 °C. In Fig. 2(a–c), selected area electron diffraction (SAED) patterns for the GP-HEA confirm the coexistence of BCC and B2 phases. Scanning transmission electron microscopy with energy-dispersive spectroscopy (STEM-EDS) elemental maps show pronounced solute partitioning, most likely associated with spinodal decomposition, where two compositional domains develop a fine grid-like pattern: one enriched in Al, Co, and Ni, and the other in Cr and Fe. This chemical modulation arises from the highly negative mixing enthalpy of Ni-Al (−22 kJ/mol) and Co-Al (−19 kJ/mol) pairs [14]. Consequently, during phase separation, Al, Co, and Ni segregate forming the B2 phase via uphill diffusion, while Fe and Cr form the disordered BCC phase [15]. The spinodal decomposition in the GP-HEA has a characteristic width of ~30 nm. Although the grain-boundary regions lack the grid-like morphology, decomposition occurs there as well, establishing an alternating banded structure with the Cr-rich BCC phase centrally located.

Fig. 2(d–f) illustrate the atomic arrangement of the B2 phase in the MP-HEA, where atoms of distinct sizes form an ordered, alternating configuration, as clearly shown in the Inverse Fast Fourier Transform (IFFT) image in Fig. 2e and consistent with previous studies [16]. STEM-EDS maps highlight a key distinction between the HEAs: solute partitioning in the MP-HEA is much finer, with a characteristic width of ~7.5 nm, roughly 25% of that in the GP-HEA. Even when materials are heat treated under exactly the same conditions, small differences in composition and/or compositional distribution (see Table 1) can still lead to noticeably different microstructural features. This is because composition directly affects two key aspects of phase separation: the thermodynamic driving force (how strongly the system 'wants' to separate, reflected in the curvature of the free energy) and diffusion kinetics (how quickly atoms can rearrange). Together, these factors determine the characteristic length scale, i.e., the wavelength of spinodal decomposition. While other influences cannot be completely excluded, the observed trend aligns well with this composition-dependent behavior.

Fig. 3a presents the evolution of hardness with aging temperature. The MP-HEA reaches a maximum hardness of 747 HV at 550 °C, which is 18.6% higher than the 630 HV achieved by the GP-HEA at the same aging temperature. Inset micrographs from higher-load indentations (296 N) reveal slight cracks in the GP-HEA, whereas the MP-HEA exhibits none, demonstrating the synchronous improvement in hardness and fracture resistance. Fig. 3(b and c) exhibit the nanoindentation load-displacement curves of these samples and their corresponding stress-strain curves. The MP-HEA exhibits higher hardness (H) and elastic modulus (E). The higher H^3/E^2 ratio of the MP-HEA (Table 2) indicates greater coating fracture resistance [17]. It is important to mention that indentation cracking and the H^3/E^2 ratio are not direct measures of the intrinsic fracture toughness, although they provide a comparative indication of fracture resistance under localized loading and are widely used in coating characterization, where conventional fracture toughness testing is not feasible. As shown in Fig. 3b, the MP-HEA requires higher loads to reach equivalent indentation depths, confirming its superior mechanical strength.

Nanoindentation compressive yield strength (YS) and power-law hardening exponent (n) are 741 MPa and 0.261 for the GP-HEA, and 1013 MPa and 0.233 for the MP-HEA (Table 2). The exponent n characterizes the strain hardening capacity of the alloy. The lower n observed for the MP-HEA indicates that plastic deformation occurs with a smaller increase in stress [18]. According to the Kocks-Mecking framework [19], strain hardening arises from the evolution of dislocation density, which results from the balance between two competing processes during plastic deformation: the storage of dislocations and their dynamic recovery (annihilation). At the early stages of deformation, dislocation storage dominates, leading to an increase in dislocation

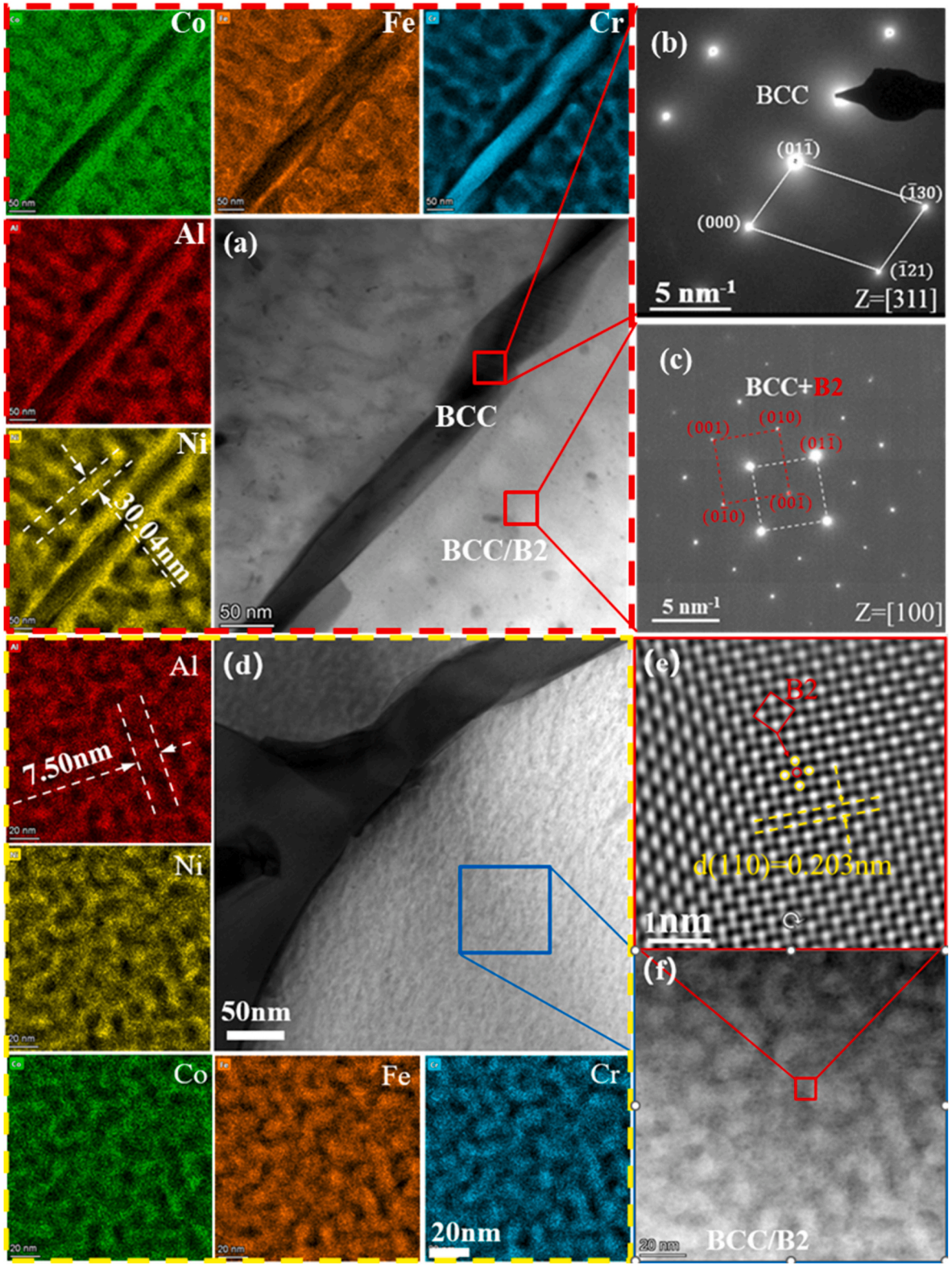

Fig. 2. TEM characterization of the AlCoCrFeNi coatings aged at 550 °C: (a-c) GP-HEA and (d-f) MP-HEA.

density and thus higher strain hardening. As deformation proceeds, however, the growing dislocation density enhances annihilation processes, so that the recovery rate progressively approaches the storage rate. This ultimately leads to a saturation of dislocation density and a corresponding decline in strain hardening. A similar tendency has been widely observed in nanostructured materials [20]. In such systems, the high density of interfaces limits the space available for dislocation accumulation and promotes recovery mechanisms, resulting in an earlier saturation of strain hardening. In the present case, the refined spinodal structure (~7.5 nm) in the MP-HEA introduces a high density of coherent BCC/B2 interfaces. These interfaces act as frequent barriers to dislocation motion, effectively reducing the dislocation mean free

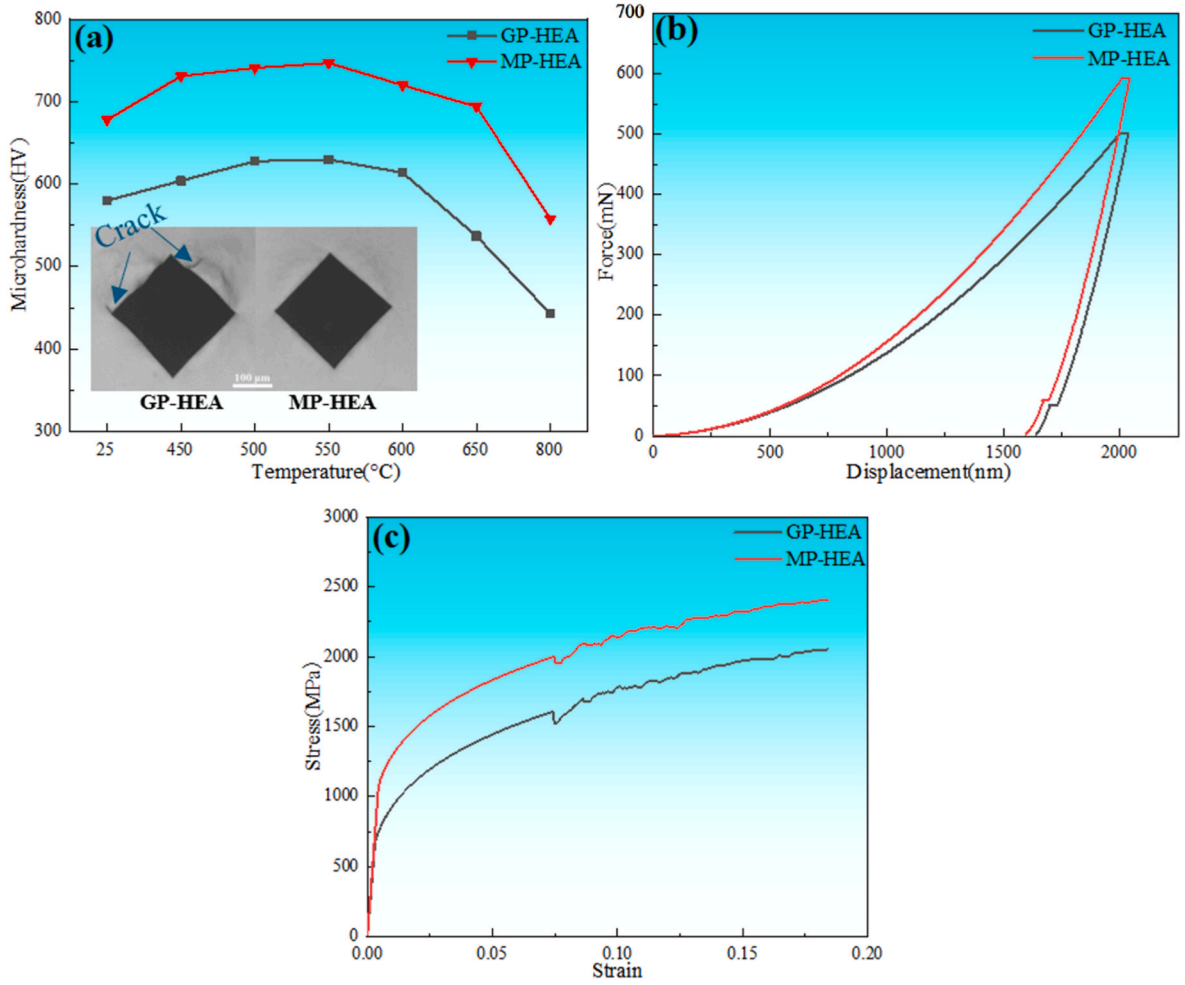

Fig. 3. (a) Vickers hardness of the GP-HEA and MP-HEA coatings as a function of aging temperature, with inset images showing representative indentations. (b) Nanoindentation load-displacement curves and (c) corresponding compressive stress–strain curves after aging at 550 °C.

Table 2
Nanoindentation-derived mechanical properties of GP-HEA and MP-HEA coatings.

HEAs	*H*/GPa	*E*/GPa	H^3/E^2/GPa	YS/MPa	*n*
GP-HEA	6.1 ± 0.1	218 ± 8	0.0048 ± 0.0004	741 ± 47	0.261 ± 0.011
MP-HEA	7.1 ± 0.1	239 ± 6	0.0063 ± 0.0004	1013 ± 60	0.233 ± 0.001

path and limiting dislocation storage. Consequently, dynamic recovery becomes significant at lower strains, leading to earlier saturation of strain hardening. This mechanism is consistent with, and likely accounts for, the observed lower strain hardening exponent (*n*) in the MP-HEA coating. Meanwhile, columnar grains in the GP-HEA coating, with their specific crystal orientation, are more prone to intergranular cracking during deformation, despite the lower strength/hardness.

4. Conclusions

The results demonstrate that powder feedstock characteristics strongly influence the microstructure. A complete CET can be achieved in the AlCoCrFeNi HEA by employing a mixed-powder feedstock during laser cladding. The induced grain refinement, together with the finer spinodal decomposition, significantly improves the mechanical response of the MP-HEA, as evidenced by increased hardness, compressive yield strength, and fracture resistance. The simultaneous improvement of these properties highlights mixed-powder processing as an effective strategy for the development of high-performance coatings.

CRediT authorship contribution statement

Yuyun Lu: Writing – original draft, Investigation, Formal analysis. **Hui Zhang:** Writing – review & editing, Supervision, Funding acquisition. **Dong Hao:** Writing – review & editing, Investigation, Formal analysis. **Ye Tao:** Writing – review & editing, Investigation, Formal analysis. **Zhenqi Dong:** Investigation. **Kaio Niitsu Campo:** Writing – original draft, Validation, Formal analysis. **Sheng Guo:** Writing – review & editing, Validation, Formal analysis, Conceptualization.

Declaration of competing interest

The authors declare that they have no known competing financial interests or personal relationships that could have appeared to influence the work reported in this paper.

Acknowledgments

This work was financially supported by the National Natural Science

Foundation of China (Grant No.51971001). The Article Processing Charge (APC) for this publication was funded by the Coordination for the Improvement of Higher Education Personnel - CAPES (ROR: 00x0ma614). For open access purposes, the authors have assigned a Creative Commons CC BY license to any accepted version of the article.

Data availability

Data will be made available on request.

References

[1] W. Li, P. Liu, P.K. Liaw, Mater. Res. Lett. 6 (2018) 199–229.
[2] J. Li, Y. Huang, X. Meng, Y. Xie, Adv. Eng. Mater. 21 (2019) 1900343.
[3] J. Menghani, A. Vyas, P. Pater, H. Natu, S. More, Mater. Today Proc. 38 (2021) 2824–2829.
[4] P. Zhang, Z. Li, H. Liu, Y. Zhang, H. Li, C. Shi, P. Liu, D. Yan, J. Manuf. Process. 76 (2022) 397–411.
[5] D. Luo, Q. Zhou, Z. Huang, Y. Li, Y. Liu, Q. Li, Y. He, H. Wang, Coatings 12 (2022) 1428.
[6] N. Gong, T.L. Meng, J. Cao, Y. Wang, R. Karyappa, C. Kiang, P. Misra, R.D.K. Misra, H. Liu, Mater. Technol. 38 (2022) 2151696.
[7] M.N. Pater, D. Qiu, G. Wang, M.A. Gibson, A. Prasad, D.H. StJohn, M.A. Easton, Scr. Mater. 178 (2020) 447–451.
[8] M. Prost, M. Köster, D. Missoum-Benziane, S. Dépinoy, L. Ferhat, M. Rambaudon, V. Maurel, Addit. Manuf. 61 (2023) 103301.
[9] H. Li, S. Thomas, C. Hutchinson, Acta Mater. 226 (2022) 117637.
[10] S. Chandra, C. Wang, S.B. Tor, U. Ramamurty, X. Tan, Nat. Commun. 15 (2024) 3094.
[11] S. Wei, P. Wang, L. Zhang, U. Ramamurty, J. Mater. Sci. Technol. 235 (2025) 133–145.
[12] H. Zhang, Y. Lu, X. Wu, J. Zhang, D. Hao, Y. Tao, L. Hu, D. Qi, K.N. Campo, S. Guo, Scr. Mater. 277 (2026) 117223.
[13] National Standardization Administration of China, GB/T 39635–2020, 2020.
[14] A. Takeuchi, A. Inoue, Mater. Trans. 41 (2000) 1372–1378.
[15] L. Zhang, D. Zhou, B.S. Li, Mater. Lett. 216 (2018) 252–255.
[16] Y. Li, Y.J. Shi, S.W. Li, X.Y. Yan, S.Y. Wang, X. Zhuo, Appl. Surf. Sci. 685 (2024) 162019.
[17] B.D. Beake, Surf. Coating. Technol. 442 (2022) 128272.
[18] T.Y. Ansell, T. Hanneman, A. Gonzalez-Perez, C. Park, A. Nieto, Part. Sci. Technol. 39 (2021) 981–989.
[19] U.F. Kocks, H. Mecking, Prog. Mater. Sci. 48 (2003) 171–273.
[20] O. Bouaziz, Y. Estrin, Y. Bréchet, J.D. Embury, Scr. Mater. 63 (2010) 477–479.